THE UNIVERSITY *of* EDINBURGH

Edinburgh Research Explorer

On the broken rotor bar diagnosis using time-frequency analysis: "Is one spectral representation enough for the characterization of monitored signals?"

OPEN ACCESS

On the broken rotor bar diagnosis using time-frequency analysis: "Is one spectral representation enough for the characterization of monitored signals?"

Panagiotis A. Panagiotou [1], Ioannis Arvanitakis [1], Neophytos Lophitis [1], Jose A. Antonino-Daviu [2], Konstantinos N. Gyftakis [1*]

[1] School of CEM, Faculty of Engineering, Environment & Computing, Coventry University, 1 Gulson Rd, CV1 2JH, Coventry, UK
[2] Instituto Tecnológico de la Energía, Universitat Politecnica de Valencia, Camino de Vera s/n, 46022 Valencia, Spain
[*] k.n.gyftakis@ieee.org

Abstract: This work enhances the knowledge on the diagnostic potential of the broken bar fault in induction motors. Since a series of studies have been published over the years regarding condition monitoring and fault diagnostics of these machines, it is essential to reach a common ground on why –sometimes– different techniques render different results. In this context, an investigation is provided with regards to the optimal window that should be adopted for the implementation of a proper time-frequency analysis of the monitored signals. On this agenda, the current paper attempts to set lower and upper bound limits for proper windowing from the digital signal processing point of view. This is done by proposing a formula for the lower limit, which is derived according to the specific frequencies one desires to put under inspection and which are the fault related signatures. Finally, a discussion on the upper bound is put onwards; results from Finite Element simulations are examined with the discussed approach in both the transient regime and the steady-state, while experimental results verify the simulations with satisfying accuracy.

1. Introduction

Induction machines are very well established in industrial environments, energy conversion systems and mobility applications. As a result, research that focuses on their condition monitoring, fault detection and diagnosis, as well as the modelling of their failure mechanisms has been going on for decades [1]-[3]. With regards to rotor condition assessment, the vast majority of diagnostic procedures relies on the analysis of frequencies with either the classical frequency domain analysis of monitored signals over the steady-state, or with the use of time-frequency (t-f) distributions during the start-up transient or other transient regimes. The first approach offers a harmonic inspection of characteristic frequency signatures and their fault sidebands visualized on a spectrum [4]-[6], whilst the second one provides the advantage of a spectral content examination through the signal's frequency trajectories and how these evolve over time. The latter are usually visualized by the means of spectrograms [7]-[9].

During actual on-field measurements, the signals handled by diagnostic engineers for the aforementioned purposes may vary: motor currents and voltages harmonic signature analyses have ushered the early diagnostic techniques of MCSA [10]-[13] and MVSA [14]-[16]; vibration, stress, torque and speed measurements lie on the foundation of the NVH (Noise/Vibration/Harshness) analysis [17]-[19]; externally radiated magnetic fields monitoring is still revealing promising results for Stray Flux Signature Analysis (SFSA) [20]-[23] and, less frequently, measurements of acoustic noise emissions are evaluated [24]-[26]. A representative literature for more detailed information on these techniques can be reviewed in [27]-[30].

To cover the most representative ones, in [11] an actual real-case scenario of induction motors in industrial environments is investigated with MCSA for broken and cracked rotors, using a threshold value of the defined diagnostic index. Broken bar diagnostics are also examined in [12] and [13] by means of current and zero-sequence current spectra respectively, which also contribute with evaluation of the fault severity according to the position of the breakages (consecutive/non-consecutive). On the other hand, [14] uses harmonic signature analysis of the line neutral voltage, while [15] introduces a similar approach for the zero-sequence voltage in wye-connected induction motors. In [16], both techniques of current and voltage signatures are tested and compared for permanent magnet synchronous machines. Moving on, aspects of vibration and noise are reviewed in [17] for electric vehicle applications, a study of spectra signatures in the vibration patterns and air-gap MMF distribution is delivered by [18] and a proposed framework for universal modelling of acoustics is depicted in [19]. Finally, [20] and [21] present the diagnostic potential of stray flux signatures for different types of faults, and the same technique with reference to its advantages is implemented in [22] and [23] during the start-up transient for rotor electrical faults and eccentricity respectively.

Furthermore, with the latest advances in digital signal processing, a breeding ground has been offered for deeper insight to the characteristics of signals and their included components. Time-frequency representations like the Wigner-Ville distribution (WVD) [31]-[33] and the Short-Time Fourier Transform (STFT) [33]-[36] provide a visualization of the squared spectral density on a lattice gridded by time and frequency, which is called the time-frequency plane and is of fixed resolution [36]-[38]. On the other hand, techniques like the Wavelet Transformation [23],

[36], [39] offer improved resolution due to the scaled tiling of the grid, but are governed from higher level of design and computational complexity [36], [39]. These methods offer a more appropriate representation than the classical FFT, since faults create time-varying conditions. The reflection of these time-varying conditions on the investigated signals is evident via the signals' spectral content evolution over time (e.g. V-shape patterns for broken bars over the transient regime [22], [23], [33], [36]). These methods however make no mention on the parameter tuning process required for proper representation, resulting in an ad-hoc selection of parameters.

With regards to the representations of fixed resolution, continuous research is published on how these techniques can be optimized and from which aspect, in order to represent results as accurately as possible. Early fundamental studies on windows are found in [40]-[42], where thorough investigation on the effect of windowing functions and their parameters is delivered in detail. More recent studies like [43]-[44] focus on the parameterization of windowing functions, while approaches for extension of the STFT are suggested in [45] for improved resolution and in [46] for adaptive windowing. In the specific case of induction machines however, taking into account the discrete nature of the investigated signals' frequency content and the system characteristics –i.e. the slip– a different, system oriented approach can be considered in the fine tuning.

On this basis, the work presented in this paper contributes into the field oriented between the parallels drawn by induction machine diagnostics and time-frequency analysis. The novelty lays within the use of a two-stage t-f analysis over the steady-state regime, to examine the known signatures induced by broken bars in the signals of stray flux. In the first stage, a short-time window is selected for the t-f representation. This selection is initially quantified by the definition of a lower bound that will result in no loss of information on the desired frequencies. At the same time, an upper bound is estimated that results in no loss of the time information that is observed in the representation of this stage. These bounds restrict and fully quantify the short-time window. In the second stage, a long-time window is selected. This selection is quantified by the estimation of a lower bound, which is expressed as a multiple of the aforementioned upper bound of the small window. These two stages are required to observe the different aspects of the effect that the time-varying conditions have in the evolution of spectral content over time. To the best of the authors' knowledge, this is the first time a small and large window concept –with bounds imposed on them– is used for the study of broken bar faults in induction machines. Furthermore, the t-f analysis is focused on the steady state and not in the transient regime, as opposed to the majority of the existing literature.

The paper is structured as follows: in Section 2, the broken bar fault signatures are briefly described from existing literature on current and stray flux measurements. In Section 3, the Short-Time Fourier Transform is reviewed and the relationship between time and frequency resolution is briefly analysed. Based on some presumable assumptions on the theoretic frequency content of the signals, a lower bound of the windowing sequence length is defined. Also, a discussion is made on the estimation of an upper bound for the small window, while the lower bound selection of a large window is justified. Section 4 presents the FEM models used for simulations and the test-bed used for the experimental measurements. In Section 5, the application of the method on results from FEM simulations is outlined, while Section 6 deals with the application on the experimental measurements. Finally, in Section 7 a conclusion on the signals' enclosed components and how they can be characterised is drawn.

2. Broken Bar Signatures

When a bar breakage occurs, the open-circuited bar generates a backward rotating magnetic field with the slip frequency. This creates an asymmetry in the airgap magnetic field and its distortions are clearly reflected in the motor's harmonic content [1], [4]-[6]. Consequently, this fault asymmetry causes additional frequency sidebands in the stator currents, separated by even multiples of the motor's slip s from the fundamental frequency f_s [13], [50]. Since every phenomenon that occurs in either the stator or the rotor is induced and filtered from one to another and vice-versa, the aforementioned sideband tones appear also in the spectrum of other stator-related quantities like the stray magnetic flux. Modulated continuously by the component $(1-s)f_s$ because of the continuous stator-rotor induction, the equation for these fault related sideband signatures is the following [6], [15]:

$$f_{bb} = \left[\frac{k}{p}(1-s) \pm s\right] f_s, \qquad (1)$$

where p is the number of pole pairs, s the motor slip and $k \in \mathbb{Z}$ such that $\frac{k}{p} \in \mathbb{Z}$. Such components are detected near the frequencies f_s, $3f_s$, $5f_s$, $7f_s$ and so on, with f_s being the fundamental supply frequency [6], [13], [15]. Since the sensor is placed on the periphery of the stator frame, it senses magnetic flux from a static point of view. Hence, the developed harmonics originate from equation (1) in accordance with the stator winding's fault related space harmonics.

A known problem in broken rotor bar diagnostics is that in large induction motors these sideband components lie usually close to the fundamental frequency due to the low value of slip s at steady state. This is highly likely to complicate the diagnostic process and make it difficult to detect the fault with accuracy, especially in cases where the load-torque oscillations are approximately equal to the sideband tones, as discerned in [50]. Therefore, in this work the sideband signatures of higher harmonics will be looked into; focus will be given to the 5th and 7th harmonic, since they are standing off at the distances $-4sf_s$ and $-6sf_s$ for the 5th and at $-6sf_s$ and $-8sf_s$ for the 7th harmonic.

3. Two stage time-frequency representation

3.1. Short-Time Fourier Transform - STFT

The windowed, or Short-Time, Fourier transform of a given signal $x(t)$ is a t-f representation and its generic form is given by the following equation [42], [48]:

$$X(t,f) = \int_{-\infty}^{+\infty} x(\tau) \cdot w(\tau - t) \cdot e^{-j2\pi f\tau} d\tau, \quad (2)$$

where $w(t)$ is the window function. In the case of a sampled and discretised signal, the discrete-time STFT [46] is given from:

$$X[t,f] = \sum_{n=t-L/2}^{t+L/2} [x_n \cdot w_{n-t}] \cdot e^{-j2\pi fnt}, \quad (3)$$

where t represents the discrete time, f is the frequency and L the window length.

As one of the most commonly applied t-f transformations, the STFT has been under study for many years and for various applications. Despite its main disadvantage of fixed resolution, as explained in [42], [48] and [49], the STFT has some robust advantages and thus is usually preferred to be applied. Such advantages are: its freedom of artefacts, avoiding the appearance of cross-terms, as well as the ability of achieving a qualitative localization in either time or frequency according to what bands of frequencies are evaluated over a fixed-time window.

3.2. T-F resolution and windowing function selection

When applying the STFT, one is called to choose a window able to capture the event of a frequency of interest or the time instants when that frequency exceeds transitions in time. Commonly, the time resolution is established previously and in practical terms is calculated from the window sequence length L_w and the sampling period T_s as follows [12], [44]:

$$\Delta t = L_w T_s. \quad (4)$$

Improved time resolution is achieved with a window of short length in time. This implies a good knowledge of the frequency's time instant, but a poor frequency resolution. Nevertheless, what is usually targeted for in the majority of the works is a compelling frequency resolution, as defined in [41], [44] and [45]:

$$\Delta f = \beta \frac{Fs}{Lw}, \quad (5)$$

β being the local equivalent noise bandwidth of the window, as defined and used in [40]-[43] and $F_s = \frac{1}{T_s}$. Improved frequency resolution is achieved with a long window in time and is known to localize better the frequency trajectory with regards to where the frequency is located. Theoretically, the concepts of time and frequency resolution are defined as spreads by the mathematical terms of the standard deviation or the root-mean-square of the signals' amplitude in time and frequency respectively [37], [48], [49]. Nonetheless, when DSP is practically applied in sampled discretized signals, (4) and (5) are used as an efficacious approximation for the calculation of Δt and Δf.

As it is apparent from (4) and (5), Δt and Δf have an inverse proportional relationship that is governed in the STFT case by the window sequence length L_w. This directly relates to the fact that it is not possible to calculate simultaneously –and with the maximum precision– the frequency and time of one harmonic included in a signal. This uncertainty relation is directly borrowed from Heisenberg's uncertainty principle [37], [38] and was introduced in the t-f analysis by Gabor [48], [49]. In the general case of t-f analysis, this uncertainty relationship is described by the inequality [37], [48]:

$$\Delta t \cdot \Delta f \geq \frac{1}{4\pi}, \quad (6)$$

Therefore, there is a trade-off between frequency and time resolution. In the majority of the time-frequency analysis tools, one must choose between computing accurately the frequency or the time when that frequency occurred. To find the best trade-off between these two resolutions, a trial and error method is usually employed.

According to [47] and [49], in order to obtain an unambiguous analysis and draw cogent conclusions on a signal and its behaviour, a t-f representation imposes to be held under both types of windows: a short one that will lead to a satisfying time resolution, and a long one that will result in a satisfying frequency resolution. The scope of this approach is not only to have a spherical view of the signals response, but also to clearly distinguish between the two different types of information comprised in a signal: a short window will give sufficient time resolution to show the modulation (FM law) and a long window will provide sufficient resolution for better localization of the frequency position, to separate a main frequency from its lower and upper sideband tones. In the same works, the authors prove that a signal can be dual-natured in terms that a predetermined time-frequency analysis does not uniquely determine the number of additional components in a signal, hence the previously described process with two different windows will reveal information about both natures of the signal: the mono-component or multi-component aspect and, at the same time, about the signal's components stationarity. This is plausible, since in the existing literature only a good trade-off for improved frequency resolution is accounted for, and this can sometimes lead to misinterpretations for distinguishing between the signal components or modulation of frequencies by a fault signature, as also explained in [50].

Another important factor for the STFT analysis is the appropriate selection of the windowing function $w(t)$. In the case of windowing functions like the Gaussian or the Kaiser-Bessel window, the STFT provides the possibility of an optimal main lobe to side lobe energy ratio. Also, these windows are known for their capability of properly analysing transients and separating signal tones with frequencies closely located to each other but with widely differing amplitudes [37], [41]. These two aspects are particularly covetable in electrical machine diagnostics, where fault conditions leave their footprint as sideband tones around main frequencies as described in Section 2.

3.3. Proposed windowing limit

According to the aforementioned aspects, in order to separate and capture the investigated frequencies, one must require a resolution Δf at least equal to the difference of the central frequency f_i from its corresponding sidebands. Hence, when applying a time-frequency analysis for broken bar diagnostics, the resolution is also dependent from the motor slip s. This is also stated in [12], where the authors explain how the sequence length –and consequently the frequency resolution– is indirectly bounded by the slip. Since these frequencies are of discrete nature though, it is possible to calculate the minimum window required for

properly distinguishing and implementing the first stage of the analysis, which is that of a short window, for the needs described in the previous paragraph.

Let $f_i \in \mathbb{R}^+$, be the i-th harmonic of the signal under investigation. As mentioned, the STFT effectively quantizes this frequency with a quantization step given by (5), into frequency $f_i^q = n_i \Delta f$, $n_i \in \mathbb{Z}^+$. The actual frequency relates to the quantized one via:

$$f_i = f_i^q + \xi_i \Delta f = n_i \Delta f + \xi_i \Delta f, \quad (7)$$

where $\xi_i \in [0, 1)$. Consider f_1 the central frequency of interest and f_2 its lower sideband. Following (7), these frequencies can be written as:

$$f_1 = n_1 \Delta f + \xi_1 \Delta f$$
and
$$f_2 = n_2 \Delta f + \xi_2 \Delta f$$

Since $f_1 > f_2$, the following relation is valid:

$$n_1 = n_2 + m, m \in \mathbb{Z}^+ \quad (8).$$

By substituting the values of n_i from (7) into (8) for both f_1 and f_2, we obtain:

$$f_1 - f_2 = (\xi_1 - \xi_2)\Delta f + m\Delta f, \quad (9)$$

where $\xi_1 - \xi_2 = \xi \in (-1, 1)$.

From (5), substituting into (9) and solving for L_w, the following is obtained:

$$L_w = \frac{\beta F_s}{f_1 - f_2}(\xi + m). \quad (10)$$

Since $m \in \mathbb{Z}^+$ defines the distance of the quantized frequencies, the minimum value of m where these frequencies are separable is $m = 1$. Also, as described in Section 2, the fault related sideband tones indicative for broken bars are distanced from a main harmonic at even multiples of the factor sf_s. Following this assumption and without loss of generality, we can set the difference $f_1 - f_2 = 2\rho sf_s$, where $\rho \in \mathbb{N}$ and (10) thereof becomes:

$$L_w \geq \frac{\beta F_s}{2\rho sf_s}(\xi + 1). \quad (11)$$

The results analysed and presented in Section 5 are based on the limit set by (11), and this limit will be applied to the Kaiser-Bessel window for the reasons explained in Paragraph 3.1. Note that in the case of a main harmonic and its upper sideband, (10) is dependant from the difference $f_2 - f_1$ and when deriving (9), one should account for $f_2 > f_1$ and $n_2 = n_1 + m$. Of course, the derived resolutions from the windows chosen by (11) will yield Δt and Δf such that the limit given by (6) will always be satisfied.

It should be noted that ξ is not a parameter that can be controlled, but is related to L_w, as ξ_1 and ξ_2 are the differences of the actual frequencies f_1, f_2 from their respective quantized ones f_1^q, f_2^q. To find the exact value of ξ to be used on (11), an exhaustive search method can be employed to minimize the selected value of ξ from the actual one after calculating ξ_1 and ξ_2 from the application of the calculated minimum L_w from (11).

Inequality (11) defines the lower bound of the short-time window. Any window length greater than that will provide the required resolution to identify the FM law without loss of information on the frequency content by assuring separability of the harmonics in a carrier-plus-

sidebands signal. A question that naturally arises is how large this window can become. As it is in the case of the frequencies, time in the STFT is also quantized by the resolution step of (4). This effectively acts as a subsampling of the original signal that is reflected on the spectrogram. It will be evident that the harmonics that will be depicted have an oscillatory behaviour under fault condition. By arbitrarily increasing L_w –thus increasing the new sampling period– there is a point at which the oscillatory behaviour will cease to be observed. This a posteriori observation, that closely relates to the time period of the oscillation, can provide with the desired upper bound on the L_w. This proposed upper bound along with (11) result in completely quantifying and defining the short-length window of the first stage.

In the second stage, a long-time window is selected to observe the frequencies over which the signal is modulated. In this case however, there is no direct imposition of either lower or upper bounds. In a worst case scenario, a selection very close to the whole time duration of the examined signal results in extracting frequency information to only one time-instant, hence the STFT degenerates into the classical FFT. The authors of [47] used such an extreme case for the quantification of the large window, where the length though was a multiple of several times larger than that of the short-time window. Based on that observation, a large window can be quantified as a multiple of the upper bound given for the short window. This ad-hoc selection of window should not exceed a specified percentage of the examined signal's duration, that will result in representing the frequencies to an adequate ad-hoc number of time instants.

## 4. Simulation models & experimental set-up

4.1. FEM models

An industrial 6-pole, $6.6\,kV$ induction motor with nominal power $1.1\,MW$ was modelled with MagNet software from Mentor/Infologic and simulated under 2D FEM rotating analysis from the start-up until the steady state. The motor operates at the supply frequency of $50\,Hz$ and the simulations are run at full load condition. The characteristics are summarized in Table 1. A population of three models has been simulated, depicted in Fig. 1 along with the spatial distribution of the magnetic flux density: the healthy motor and two motors with broken bars. To aid the reader, the three motors are labelled and referred to as Model #1 – Model #3. The models are summarized in Table 2, where the slip value of each motor is given in the last column. As shown in Fig. 1a, the stray flux sensor is located

Table 1 FEM model characteristics

Characteristics	
Rated Power	1.1 MW
Supply Frequency	50 Hz
Rated Voltage	6.6 kV
Rated current	170 A
Rated Speed	990 rpm
Stator winding connection	Y
Number of pole pairs	3
Number of rotor bars	70
Number of stator slots	54
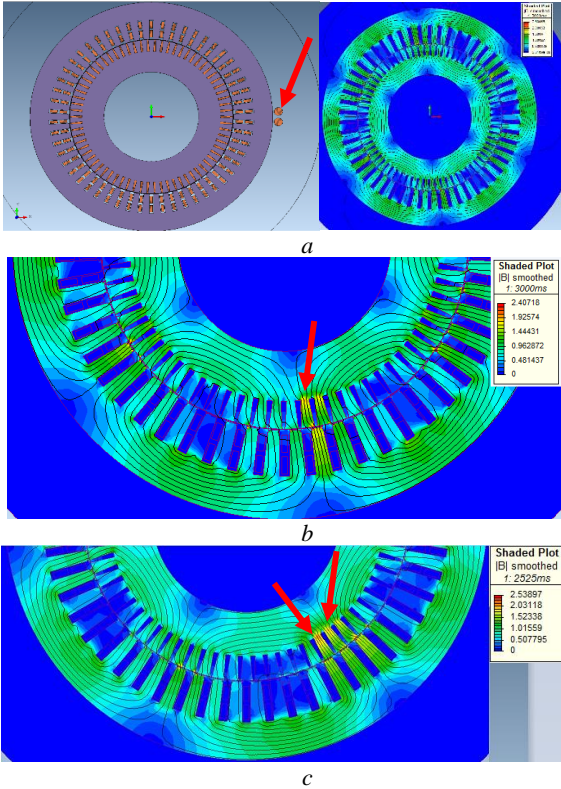
Fig. 1. *FEM models of the 1.1 MW motor:* (**a**) Solid healthy model (left) and spatial distribution of the magnetic flux density (right), (**b**) magnetic flux density spatial distribution under single bar fault (**c**) magnetic flux density spatial distribution under two adjacent broken bars

at the machine's right hand-side accounting for radial stray flux (red arrow). Consisting of a wounded rigid search-coil of 100 turns, to capture spreading magnetic fields (leakage flux) on the machine's peripheral area. The red arrows in Fig. 1b and Fig. 1c point the location of the broken bars.

Table 2 Summary of simulated cases

Case	Model	slip
Healthy	*#1*	*0.0089*
1 br. bar	*#2*	*0.0090*
2 adjacent br. bars	*#3*	0.0095

The models were simulated under the same simulation type, that is Transient-2D with motion analysis which is a rotary load-driven motion accounting for the machine's motion equation and the initial moment of inertia from the start-up until the steady state. The simulations are run at full load condition. To obtain a fair sample of data, both the healthy model as well as the models with broken bars were simulated for approximately 7.5 seconds with a sampling frequency of $5\,kHz$.

4.2. Experiments

The motor used for experimental validation of the proposed approach is a 4-pole, $230\,V$, $1.1\,kW$ laboratory induction motor. The broken bar fault was achieved by drilling holes of small depth in the bars of a healthy rotor and by implementing this rotor on the same stator. Also, the flux sensor was used as in the case of the FEM models, wounded on the machine's periphery and held on the stator's housing, connected with a data acquisition system

sampling at the frequency of $5\,kHz$, accounting for radial stray flux signals. The experimental test-bench of the induction motor topology, as well as the different rotors used for emulating the broken bar fault are shown in Fig. 2.
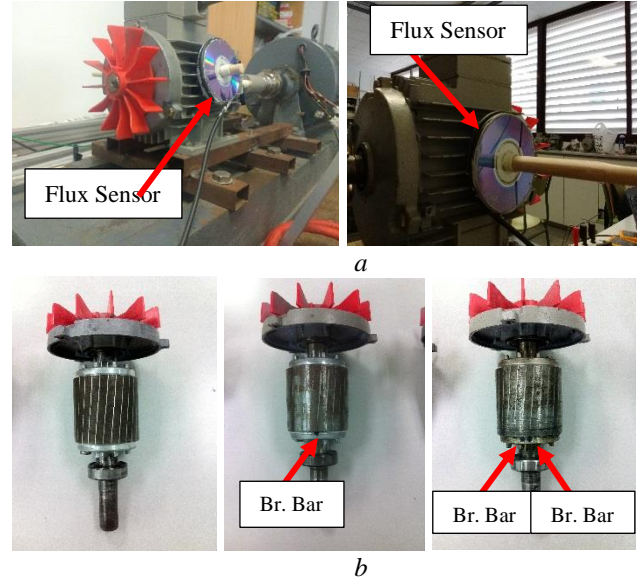
Fig. 2. *1.1 kW motor used for the experimental tests* (**a**) Stray flux sensor in different positions, (**b**) healthy rotor (left), rotor with one broken bar (middle) and rotor with two adjacent broken bars (right)

The motor's characteristics, as given by the motor's nameplate, are summarized in Table 3 and all the tested cases with their slip value in Table 4. Starting with the healthy motor and in accordance with the FEM models, the experimental cases are labelled and referred to as Motor #1 – Motor #3 respectively and are also tested at full load.

Table 3 Experimental motor characteristics

Characteristics	
Rated Power	1.1 kW
Supply Frequency	50 Hz
Rated Voltage	230 V
Rated current	4.5 A
Rated Speed	1410 rpm
Stator winding connection	Δ
Number of pole pairs	2
Number of rotor bars	28
Number of stator slots	36

Table 4 Summary of experimental cases

Case	Motor	slip
Healthy	*#1*	*0.0121*
1 br. bar	*#2*	*0.0124*
2 adjacent br. bars	*#3*	0.0128

5. Analysis of the FEM Simulation Results

In Table 5, the first column provides the sideband components that are investigated for the different values of ρ, for each harmonic as given from (11). Although the value of $\rho = 2$ separates the central frequency from each one of its sidebands, the spectrograms are derived for $\rho = 1$, since $\rho = 1$ will separate every component distanced at least

$2sf_s$ from each other. In the second column, the absolute value (distance) of each sideband harmonic is given in Hz (freq. resolution), while the last column gives the value of L_w, calculated by the limit of (11). Finally, the equivalent noise bandwidth of the window is given in every case.

Table 5 Model #2: investigated sidebands & calculated window length for the case of a single bar fault

| Case	1 Broken Bar	Window
$\xi = -0.5$	$s_2 = 0.0090$	$\beta = 1.83$
Sideband	*Frequency (Hz)*	L_w
$2sf_s\ (\rho=1)$	0.9	**4326**
$4sf_s\ (\rho=2)$	1.8	2548
$6sf_s\ (\rho=3)$	2.7	1698
$8sf_s\ (\rho=4)$	3.6	1274

The choice of $\xi = -0.5$ was achieved by tuning with parameter sweeps in the set $(-1, 1)$ under a step of 0.01 between the sweeps. From the set of windows yielded (Table 5), the largest of the set is used ($L_w = 4326$) for deriving the investigated spectrograms for two reasons: in a visualization manner, for the best trade-off for improved frequency resolution under the condition of a short window and, secondly, to allow the window and span several cycles of the lowest modulating frequency enclosed in the original signal [47], since separability of the components has already been accounted for by (11) in any case of the used window. Similarly, Table 6 presents the investigated components and the ρ values along with the minimum required L_w and the calculated equivalent noise bandwidth.

Table 6 Model #3: investigated sidebands & calculated window length for the case of adjacent broken bars

Case	2 Adjacent Broken Bars	Window
$\xi = -0.5$	$s_3 = 0.0095$	$\beta = 1.83$
Sideband	*Frequency (Hz)*	L_w
$2sf_s\ (\rho=1)$	0.95	**4226**
$4sf_s\ (\rho=2)$	1.9	2414
$6sf_s\ (\rho=3)$	2.85	1609
$8sf_s\ (\rho=4)$	3.8	1207

For a comprehensive comparison between all the faulty motors' stray flux spectral characteristics the analysis should first include an examination of the healthy motor's stray flux signals. Fig. 3 depicts the extracted spectrograms of the radial stray flux measured in the healthy motor (Model #1) under both types of window for the given dataset. Each subfigure focuses on the frequency area of interest: the 5th harmonic (Fig. 3a, 3b) and the 7th harmonic (Fig. 3c, 3d), where with improved localization in either time or frequency, one can easily conclude on the same observation, thus being the non-existence of the investigated sidebands. Neither the $(5-4s)f_s$ and $(5-6s)f_s$, nor the $(7-6s)f_s$ and $(7-8s)f_s$ trajectories exist in the motor. These spectrograms are to be used as a baseline for the rest of the cases and also to denote that for a machine in healthy condition, the spectral signatures' trajectories are of flat morphology and without undergoing any modulations during the steady-state regime. Nevertheless, a machine operating under the existence of a fault is practically operating in time-varying conditions [51]-[54]. In the case of stray flux signature analysis, these time-varying conditions' periodicity is designated according to the fault periodicity over the rotation of the rotor and the continuous induction of electromagnetic quantities from the stator to the rotor and vice-versa [28], [52]-[54]. Such periodicities are not always easy to track through the frequency spectra; therefore a time-frequency representation –where they are translated on a spectrogram as modulations, as demonstrated in following Fig. 4 and Fig. 6– provides


a

b

b

b
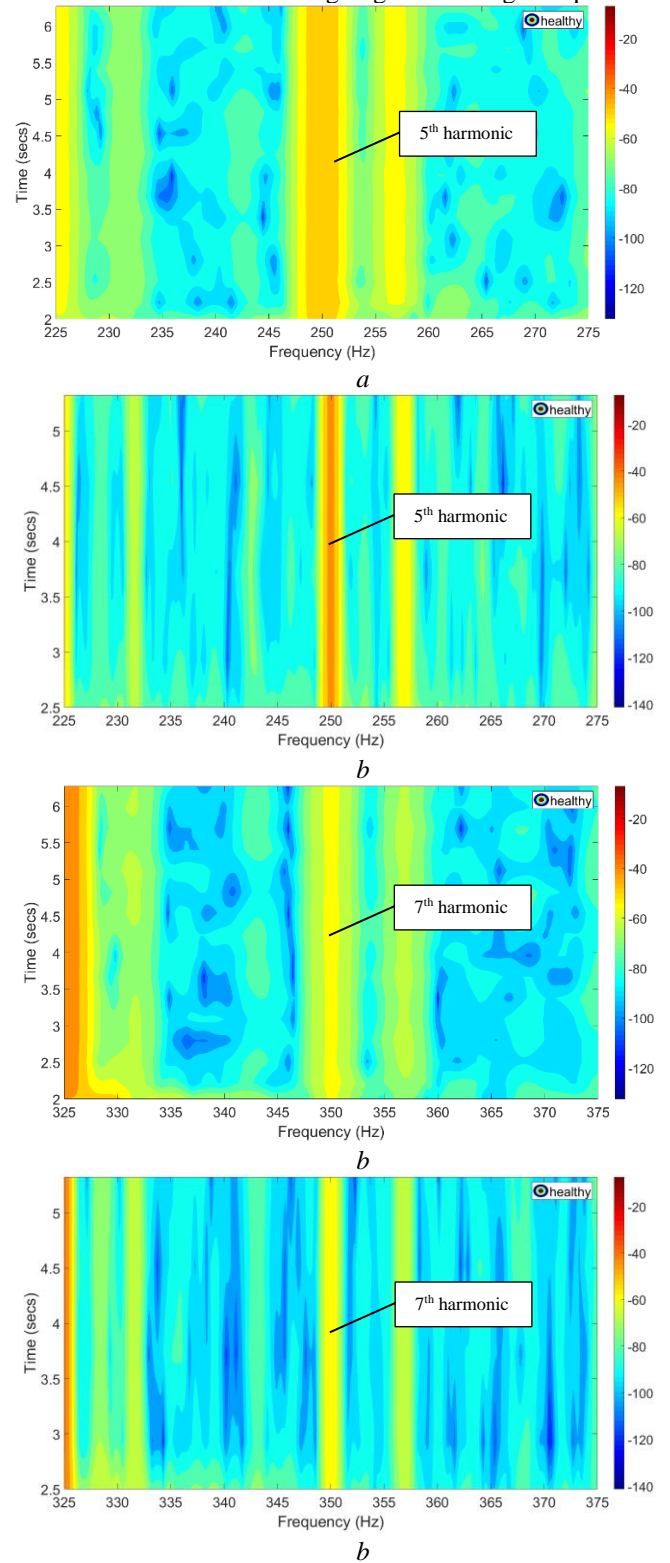
Fig. 3. *Harmonics of interest for Model #1 (healthy):*
(a) 5th Harmonic under a short-term window **(b)** 5th Harmonic under a long-time window **(c)** 7th Harmonic under a short-term window **(d)** 7th Harmonic under a long-time window

clearer indications for the fault condition on the pipeline for a diagnostic decision, in cases where using the classical FFT like the MCSA might fail to do so due to loss of diagnostic information, as explained in [53]-[55].

In Fig. 4, the spectrograms corresponding to the 5th harmonic (Fig. 4a) and the 7th harmonic (Fig. 4b) are shown for Model #2. Although the selected window resolves the modulation sufficiently enough to observe its characteristics, the sideband tones cannot be visually discriminated easily. However, due to (11) the frequency spread has been bounded to be such that for the aim of the analysis, any existing amplitude oscillations are also discriminated. A closer look in the frequency band of the 5th harmonic (circled in dashed) clearly spots a multi-tone FM signal with non-stationary characteristics and the carrier getting strongly modulated over the first 3.5 seconds. From 3.5 seconds and onwards, the spectrogram admits a multi-tone FM signal with more stationary characteristics over time and which encloses a modulated carrier with modulated components with a dominant period ranging around $0.95 - 1.1\ sec$, evident in the areas highlighted with dashed circles. The same observations apply for the band of the 7th harmonic, with the difference that the modulation taking place in the components is of a slightly increased period compared to the 5th harmonic. Most of these characteristics are also evident on the spectrograms of the stray flux signals from the experiment.
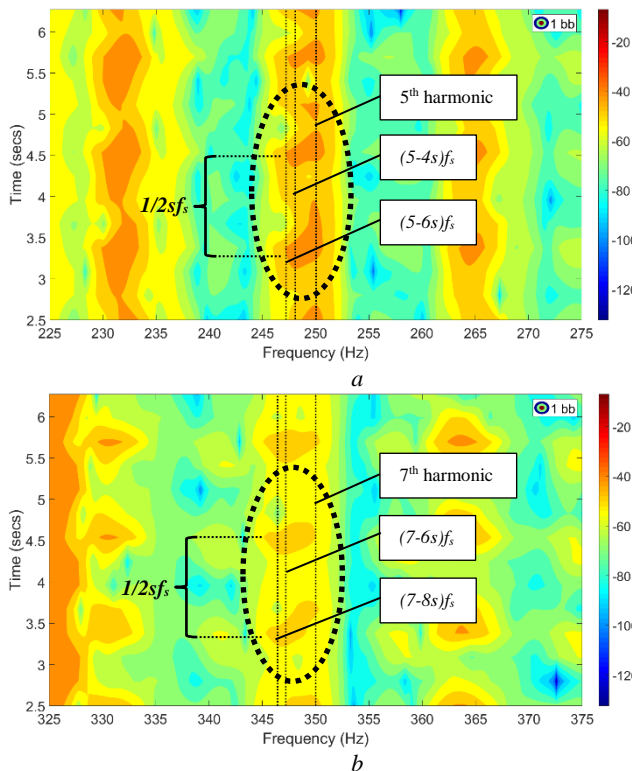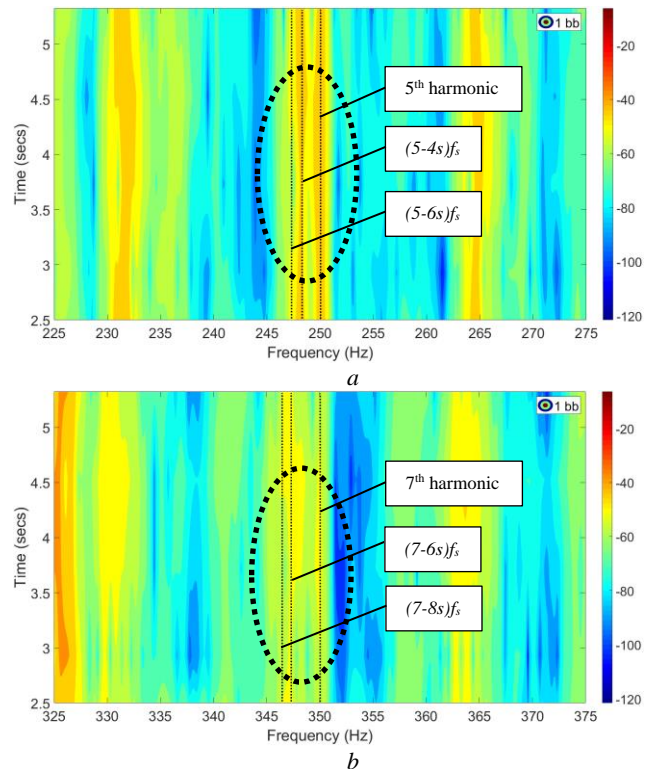

Fig. 4. *Harmonics of interest for Model #2 captured with the minimum required L_w as calculated from the proposed limit:* **(a)** *area of (5–4s)fs and (5–6s)fs* **(b)** *area of (7–6s)fs and (7–8s)fs*

With the observations on the frequency oscillations made from the utilized minimum length window, an upper bound on the window length can be defined, as explained in Paragraph 3.3. As seen in Fig.4 these oscillations have a period in the area of $0.95 - 1.1\ sec$, without exceeding this interval. By considering that the sub-sampling must not result in loss of information, according to Nyquist, the new

sampling period -and hence the window length- should not exceed the half of the oscillations' period, which in our case is around $0.55\ sec$. By considering equation (4) and that the original signal's sampling period is $T_S = 0.2\ msec$, the upper bound of the short-time window is given from inequality $L_w \leq 7250$. It should be noted that this is a rough estimation, as the periods of the modulating signals were extracted in a visual manner. To compensate for this, the case of the lowest possible period is selected.

From this upper bound, the long-time window of the second stage can be defined, as a multiple of the upper bound. On the other hand, this multiple cannot be multiplied and increased arbitrarily, because it also depends on the original signal's length. If a window 9-10 times larger than the lower bound was to be considered, it would result in a window of larger than the actual length of our signal which is $L_{total} = 43000$. In this case the long-time window used is of length $L_w = 19750$, which is a window approximately 3 times the short-time window's upper bound. Fig. 5 indicates the existence of a multi-component and stationary signal. Although the resolution in frequency is very well improved, it cannot resolve the modulation with accuracy in the visualization manner like in Fig. 4. Hence, their amplitude can better be evaluated at this point, but not their periodicity. The carrier-plus-sideband form of the examined signal encloses a modulated carrier with unmodulated components for the 5th harmonic's band (Fig. 5a) and for the 7th harmonic's band (Fig. 5b).
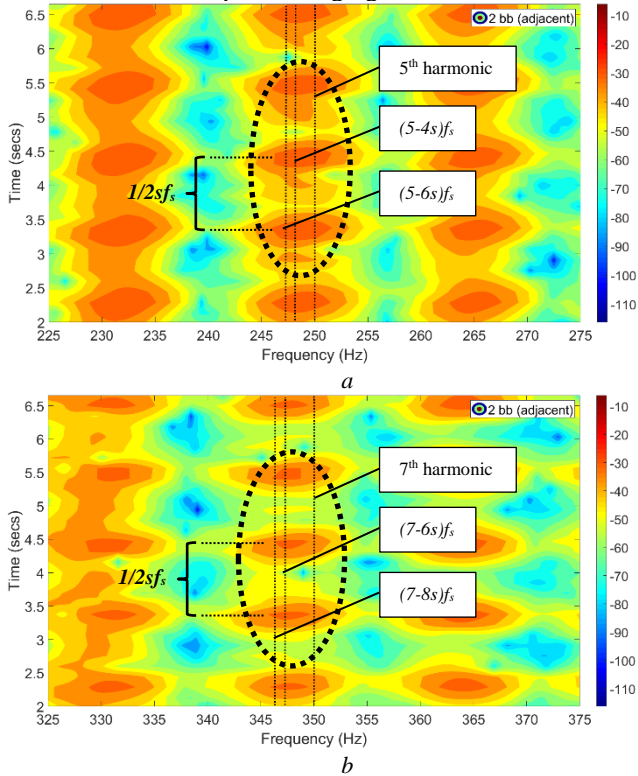

Fig. 5. *Harmonics of interest captured with the long-time window for Model #2:* **(a)** *area of (5–4s)fs and (5–6s)fs* **(b)** *area of (7–6s)fs and (7–8s)fs*

The observations made on the spectrograms of Fig. 4 and Fig.5 are coming in agreement with the statements made in [47] and [49] that a signal is usually governed by duality in its nature when susceptible to time-varying conditions, i.e. operation under fault existence. With respect to that, the

7

harmonics examined in this Section indeed imply the existence of a non-stationary multi-component signal over the transient regime, while the same harmonics indicate to be included in a multi-component quasi-stationary signal during the steady-state. Also, as increasing the frequencies range and looking into this band of higher harmonics, spectral density oscillations are more evident and amplitudes modulation is indicative of more spectral energy concentration in the sidebands.

Furthermore, Fig. 6 and Fig. 7 show the spectrograms for Model #3 in the frequency areas of interest, extracted with the window of the first stage and the window of the second stage respectively. Since this is a case of broken bars at adjacency, the observed modulations are similar to those of the single bar fault. However, the investigated modulations admit a period ranging between 1.1 sec and

Fig. 6. Harmonics of interest for Model #3 captured with the minimum required L_w as calculated from the proposed limit: **(a)** area of $(5–4s)f_s$ and $(5–6s)f_s$ **(b)** area of $(7–6s)f_s$ and $(7–8s)f_s$

1.15 sec (circled in dashed). Considering the fault related speed-ripple component at $2sf_s$, generated by the sequence described in [28] and [50] from the two counter-rotating magnetic fields in the point of breakage and which is only present in faulty rotors, it is found to be at $0.95\,Hz$ for Model #2 and $0.9\,Hz$ for Model #3. Accounting for $1/2sf_s$ in each motor, the speed ripple component manifests itself on the examined modulations' periods, since it is at 1.05 sec for Model #2 (modulation periods $0.95{\sim}1.1\ sec$) and 1.11 sec for Model #3 (modulation periods $1.1{\sim}1.15\ sec$). This allows to report that higher frequencies' ranges, like the ones examined in this work, show a compelling diagnostic potential when using the proposed approach of a t-f analysis in two stages. This validates even further the fact that information originating from the time-varying nature of the fault is vulnerable to be lost in a classical frequency domain approach. On the other hand, a t-f representation without system oriented fine tuning of parameters –which in

this case relate to the slip and sampling frequency– might also result in information loss.
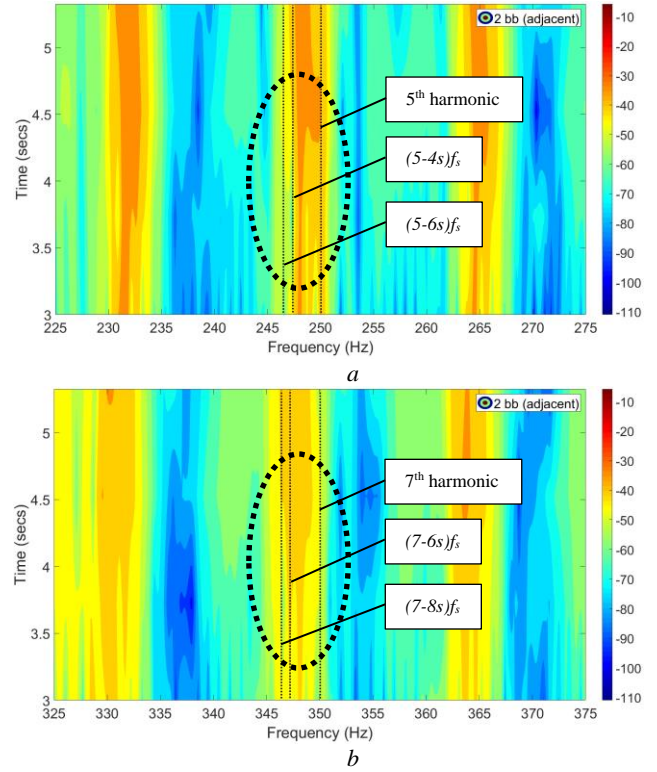
Fig. 7. Harmonics of interest captured with the long-time window for Model #3: **(a)** area of $(5–4s)f_s$ and $(5–6s)f_s$ **(b)** area of $(7–6s)f_s$ and $(7–8s)f_s$

It should also be noted that, the approach of this system oriented parameter tuning can be used for t-f process like the ones described in [32]-[34] or [53]-[57] as an initialization pre-setting and fine tuning; it is also eligible to define the two extreme limits where these methods or similar types of analyses can be tested, when aiming to extract different pieces of information in two stages. At one of these extremes shown in Fig. 7 –under a long-time window for Model #3– the aforementioned modulations patterns have ceased and are no longer visible, as the trajectories are better localized in frequency, thus allowing to observe a different aspect of the localized fault at improved resolution for amplitudes examination.
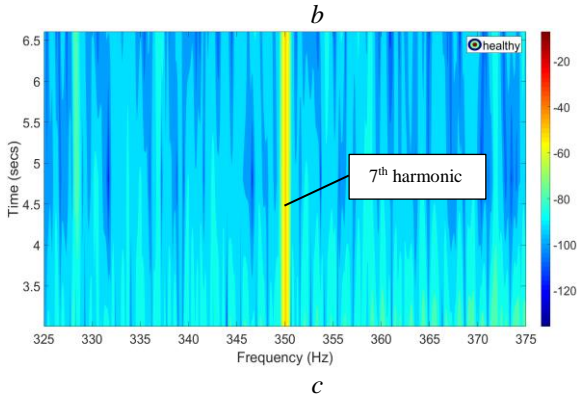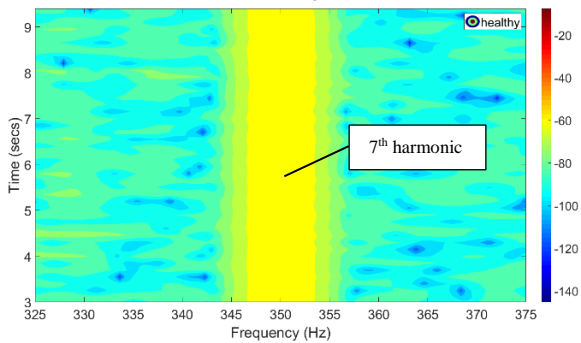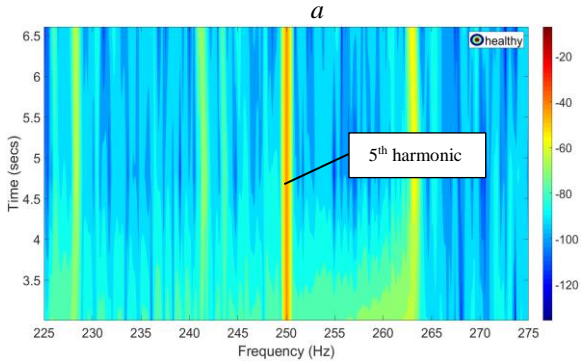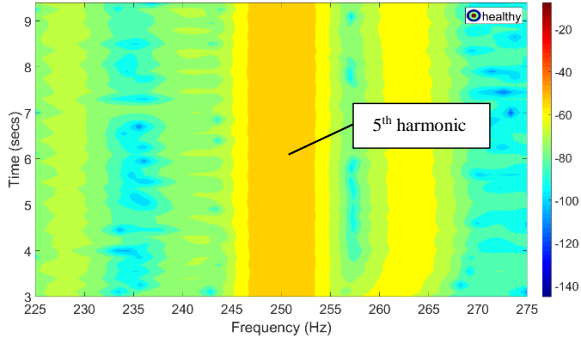
6. Analysis of Experimental Results

Regarding the experiments, as it is shown in Table 7, the slip of the motor with one broken bar being $s_{m2} = 0.0124$, while the slip of the motor with two broken bars is $s_{m3} = 0.0128$ (Table 8). In accordance with Table 3 and Table 4, the first column provides the sideband components that will be looked into for the different values of ρ for each harmonic as given from (11).

As in the case of the FEM simulations' results, the healthy motor's spectrograms are demanded to examine the existence of the sideband signatures and decipher any nearby components in the area of the 5th and 7th harmonic respectively. These are shown in Fig. 8 where it is clear that a healthy rotor is dealt with, since the vacancy in the frequency areas of the 5th and 7th harmonic justifies the absence of components indicating true negative diagnosis for rotor electrical faults.

8

Table 7 Motor #2: investigated sidebands & calculated window length for the case of adjacent broken bars

Case	1 Broken Bar	Window
$\xi = -0.8$	$s_3 = 0.0124$	$\beta = 1.98$
Sideband	*Frequency (Hz)*	L_w
$2sf_s\ (\rho=1)$	1.24	**3505**
$4sf_s\ (\rho=2)$	2.48	2003
$6sf_s\ (\rho=3)$	3.72	1336
$8sf_s\ (\rho=4)$	4.96	1002

Table 8 Motor #3: investigated sidebands & calculated window length for the case of adjacent broken bars

Case	2 Adjacent Broken Bars	Window
$\xi = -0.8$	$s_3 = 0.0128$	$\beta = 1.98$
Sideband	*Frequency (Hz)*	L_w
$2sf_s\ (\rho=1)$	1.28	**3397**
$4sf_s\ (\rho=2)$	2.56	1941
$6sf_s\ (\rho=3)$	3.84	1294
$8sf_s\ (\rho=4)$	5.12	970

Fig. 9 depicts the spectrograms with the windowing sequence length calculated from (11) for Motor #2. Since this windowing limit has yielded shorter windows in time, the time resolution of these spectrograms is improved compared to Fig. 3. This means that the FM law is better localized and able to be observed. The trajectory of the 5th harmonic oscillates over the first 2 *sec*, but its transient is much more smoothed with respect to the widely ranging amplitude of the central frequency and its sideband tones. Although the stationarity is less present and the amplitude ripple of an approximately 0.8 *sec* period, still the tone modulation of the main component and its components is observable. Furthermore, the spectrogram of the 7th harmonic is enclosing sidebands with oscillating amplitudes, as the ripples dotted over time show. This means that the average value of the squared spectral density undergoes ripples due to an AM modulation of the fault signatures. The energy concentration is approximately constant for both, but their difference in amplitude range is very clear. This indicates the existence of a multi-tone FM process with non-stationary characteristics (Fig. 9a), as the main component
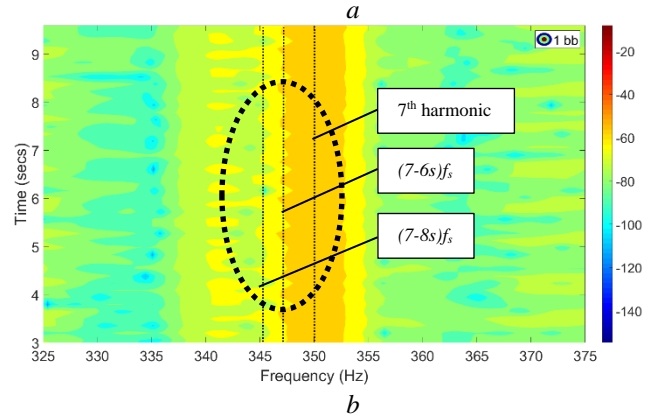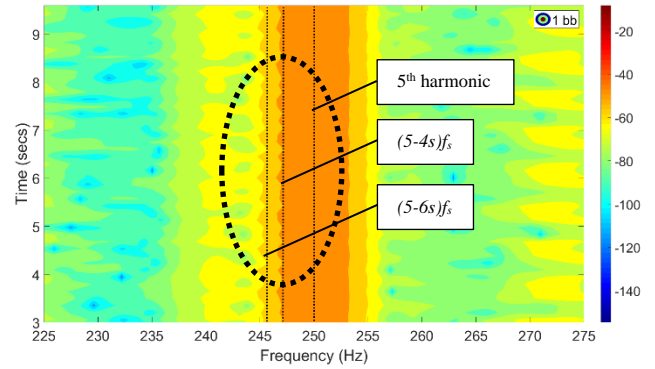

a

b

b

c

Fig. 8. *Harmonics of interest for Model #1 (healthy):*
(a) 5th Harmonic under a short-term window and **(b)** under a long-time window, **(c)** 7th Harmonic under a short-term window and **(d)** under a long-time window

a

b

Fig. 9. *Harmonics of interest for Motor #2 captured with the minimum required L_w as calculated from the proposed limit:* **(a)** area of $(5–4s)f_s$ and $(5–6s)f_s$ **(b)** area of $(7–6s)f_s$ and $(7–8s)f_s$

aspect is characterized by the widest amplitude, while Fig. 9b reveals a multi-component aspect which is also non-stationary, but uniformly spread regarding its energy. In accordance with [47], this duality in the nature of the frequency trajectory raises questions, on whether a time-frequency analysis under one condition of improved resolution is advocate enough to characterize a fault condition and draw straight-forward conclusions upon it.

Examination of the same harmonics under a long window in time (improved frequency resolution) localizes the so called frequency position and this localization spots the trajectory's value and rise in amplitude as the modulating component. The long-time window in this case, was accounted for similarly with the case of the FEM simulations, as a multiple of the short-time window's upper bound. Since the oscillations present in the harmonics of the spectrograms in Fig. 9 are of the period $0.75\sim0.85\ sec$ for Motor #2, it is easily calculated that the short window's upper bound is $L_w \leq 8125$. Having available an extended measurement though, the signals in this case are of the length of $L_{total} = 250250$. This allows us to multiply the upper bound several times more, hence the window used for the second stage of the analysis is of length $L_w = 25025$ data points, which is a windowing of 12 segments and which is an adequate number of time instants, while at the same time providing a good frequency resolution of $\Delta f \approx 0.28$ Hz, as calculated from (5).


a

b
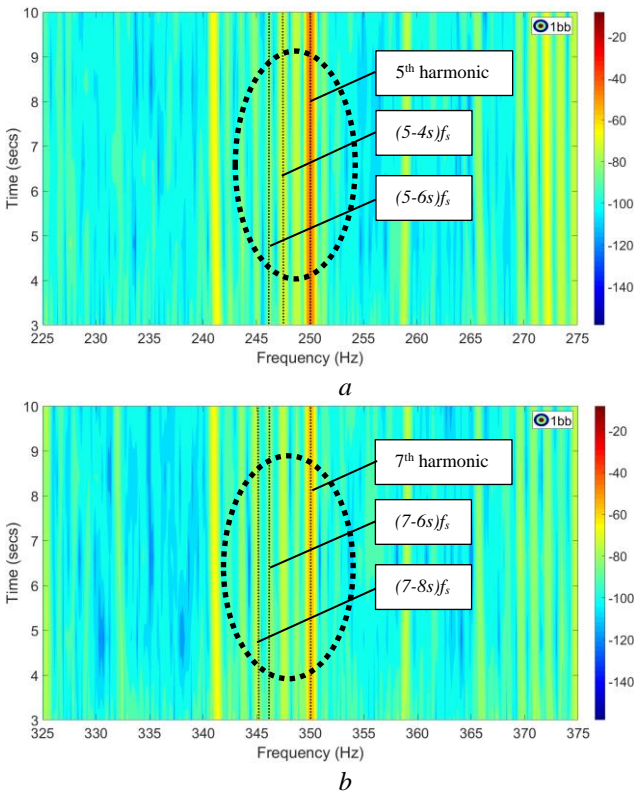
Fig. 10. *Harmonics of interest captured with the long-time window for Motor #2:* **(a)** *area of (5–4s)fₛ and (5–6s)fₛ* **(b)** *area of (7–6s)fₛ and (7–8s)fₛ*

The modulated stationary carrier depicted in Fig. 10a and Fig. 10b and its amplitude ranging modulated neighbouring components agree with those of Fig. 5a and Fig. 5b. The notable difference in the amplitude levels of the harmonics between Fig 5 and Fig. 10 is due to the size and power rating difference of the two machines. Apparently,

the larger machine's stray flux signals emerge on the search coils after spreading with larger amplitudes.

As it is also put and asked for in [47] and [49], the question is how well the terms of stationarity and mono or multi-component aspects are well defined to equip us with robust criteria and allow us to fully characterise signals, something that is very important during the discrimination of faults and diagnostics by frequency signature inspection. Another issue addressed, is how long should be the windowing sequence, in order to localize frequencies well but without totally obscuring the information of time and vice-versa. In other words, the two-step analysis proposed in this work provides an advantage when investigating fault frequencies and categorizing the two different behavioural aspects of a signal.

Finally, Fig. 11 shows the spectrograms with the short-term window calculated from (11) for the stray flux signals of Motor #3. On the same basis with the FEM models in Section 5, since $s_{m3} = 0.0128$ and the $2s_{m3}f_s = 1.28\ Hz$, it is seen that the modulations of Fig. 11 are again designated with a period of $0.8\ sec \approx \frac{1}{2s_{m3}f_s} \approx 0.78\ sec$. Exactly as in the FEM cases, this was also the case for Motor #2 (Fig. 9), where the modulations' periods were $0.75\sim0.85\ sec$ as the speed ripple component at $2s_{m2}f_s = 1.24$ introduces a modulation of period $\frac{1}{2s_{m2}f_s} \approx 0.81\ sec$. Finalizing the analysis under a long-term window for the given dataset, in Fig. 12 the spectrogram under improved resolution in frequency ($\Delta f \approx 0.28$ Hz) is shown, where the speed-ripple designation is no longer visible due to localization in frequency. At the representation of this stage, improved resolution spectrograms like the ones presented in Fig. 10 and Fig. 12 can be used for examination of the trajectories

a

b
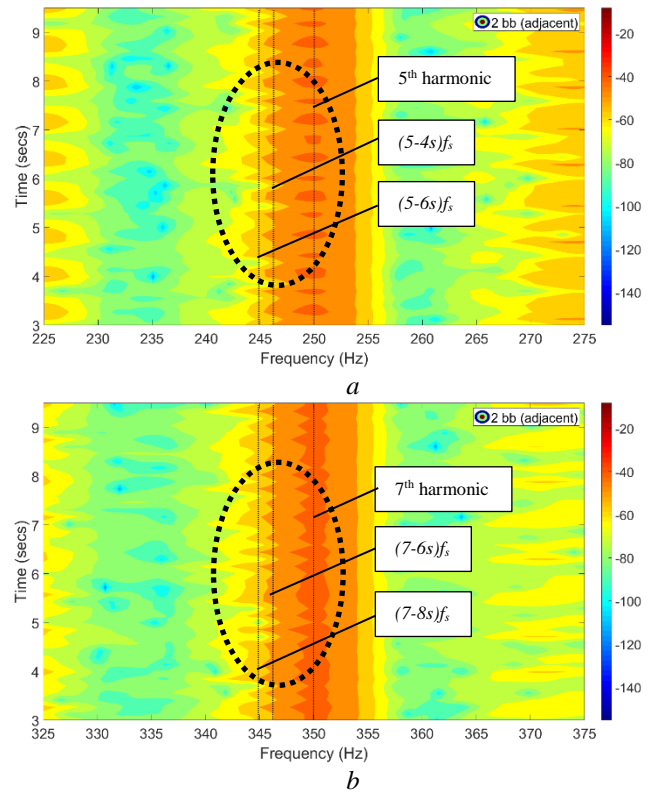
Fig. 11. *Harmonics of interest for Motor #3 captured with the minimum required Lₓ as calculated from the proposed limit:* **(a)** area of *(5–4s)fₛ and (5–6s)fₛ* **(b)** area of *(7–6s)fₛ and (7–8s)fₛ*

and evaluation of their amplitudes over time. In any case, localization in frequency resolves the exact position of the fault trajectories, validating their distance from each other as well as the main harmonic (5th or 7th in this case), in order to evaluate their amplitudes ranges. However, how these respond in FM terms can reveal an alarming notice as well, when studied under a short-term window for a fault condition, as presented in the first stage of the discussed approach.
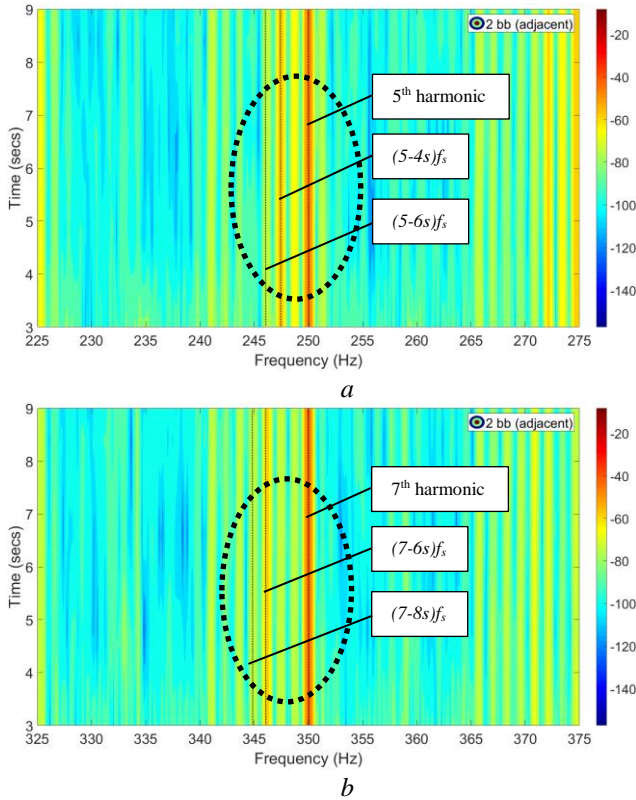
Fig. 12. *Harmonics of interest for Motor #3 captured long-time window:* **(a)** *area of (5–4s)f_s and (5–6s)f_s* **(b)** *area of (7–6s)f_s and (7–8s)f_s*

7. Conclusion & Discussion

This work presented a two stage t-f analysis using the STFT under the Kaiser-Bessel window, for the evaluation of stray flux signals regarding their carriers and modulated components at fault signatures of broken bars and their sideband tones. The frequency signatures and their behaviour were studied and characterized at this fault condition by examining both types of information carried in the harmonics designated by the fault. Having defined a proposed minimum required window length to obtain advocate resolutions on the t-f plane according to the motor's slip, the response of stray flux signals has been put under inspection for two harmonic signatures and their fault sidebands (5th, 7th). Initially, evaluation of the localized time response (improved time resolution), reveals the existence of a strong FM signal with a changing personality though regarding the amplitude modulation over the frequencies transitions. As a second step, the same harmonics were examined with improved frequency resolution to evaluate the amplitude response of the better localized frequencies. The same behaviour was also observable when a posteriori examined under a long-time window condition, a case where

the examination of the amplitude's ranges and spectral energy concentration was evaluated.

Both from the simulation results and the experimental ones, the signal characterization implies that existing duality in signals' nature is a fact, mainly under fault conditions. To exploit and overcome this at the same time, an analysis of the signals in a two-stage manner can provide -like in the case of the mentioned literature- advantages for diagnostic purposes like the broken bar fault in induction motors. The reported findings help the signal characterization during this fault condition, and enhance the discrimination of existing phenomena like the fault related slip and speed oscillations over the steady-state regime.

Having the disadvantage of fixed resolution, the STFT analysis is still to be investigated under adapting windowing. Also, since the ξ parameter is subject to optimization, further future research aspects on this matter may include the selection of ξ by the application of an optimization or a grid search algorithm, aiming to the examination of a time-varying window after extraction -if possible- of the instantaneous frequency information.

8. Appendix

Flux Sensor Characteristics
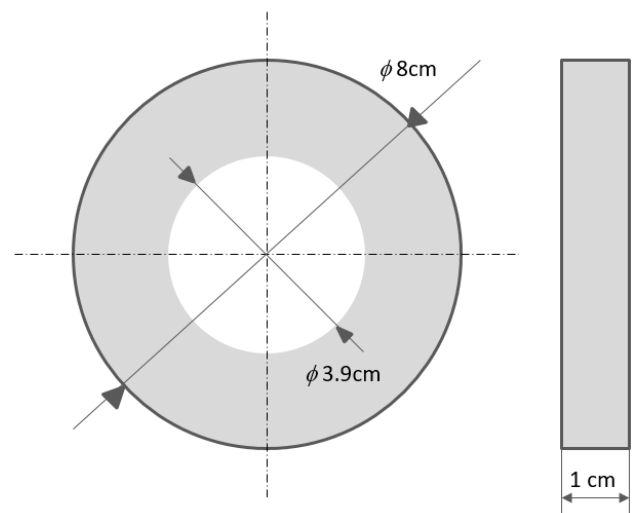
Magnetic flux sensor, 1000 turns, 1cm slot thickness, $\phi_{internal} = 3.9$ cm, $\phi_{external} = 8$ cm.

9. References

[1] Penman, J., Stavrou, A.: 'Broken rotor bars: their effect on the transient performance of induction machines', IEE Proceedings – Electric Power Applications, Vol. 143, No. 6, pp.449-457, Nov. 1996.

[2] Joksimović, G. M., Riger, J., Wolbank, T. M., Perić, N., Vašak, M.: 'Stator-Current Spectrum Signature of Healthy Cage Rotor Induction Machines', IEEE Transactions on Industrial Electronics, Vol. 60, No. 9, pp. 4025-4033, Sept. 2013.

[3] Gritli, Y., Bellini, A., Rossi, C., Casadei, D., Filippetti, F., Capolino, G. A.: 'Condition monitoring of mechanical faults in induction machines from electrical signatures: Review of different techniques', IEEE 11th International Symposium on Diagnostics for Electrical Machines, Power Electronics and Drives (SDEMPED), pp. 77-84, Aug. 2017.

[4] Bellini, A., Flippetti, F., Franceschini, G., Tassoni, C., Kliman, G. B.: 'Quantitative evaluation of induction motor broken bars by means of electrical signature analysis', IEEE Transactions on Industry Applications, Vol. 37, No. 5, pp. 1248-1255, Sep. 2001.

[5] Henao, H., Demian, C., Capolino, G. A.: 'A Frequency-Domain detection of stator winding faults in induction machines using an external flux sensor', IEEE Transactions on Industry Applications, Vol. 39, No. 5, pp. 1272-1279, Sept. 2003.

[6] Eltabach, M., Charara, A., Zein, I.: 'A comparison of external and internal methods of signal spectral analysis for broken rotor bars detection in induction motors', IEEE Transactions on Industrial Electronics, Vol. 51, No. 1, pp. 107-121, Feb. 2004.

[7] Supangat, R., Ertugrul, N., Soong, W.L., Gray, D.A., Hansen, C., Grieger, J.: 'Detection of broken rotor bars in induction motor using starting-current analysis and effects of loading' IEE Proceedings – Electric Power Applications, Vol. 153, No. 6, pp.848-855, Nov. 2006.

[8] Wang, C., Zhou, Z., Unsworth, P. J., Igic, P., 'Current space vector amplitude fluctuation based sensorless speed measurement of induction machines using Short Time Fourier Transformation', 34th Annual IEEE Industrial Electronics Conference (IECON'08), pp. 1869-1874, Nov. 2008.

[9] Lopez-Ramirez, M., Romero-Troncoso, R. J., Morinigo-Sotelo, D., Duque-Perez, O., Ledesma-Carrilo, L. M., Camarena-Martinez, D., Garcia-Perez, A., 'Detection and diagnosis of lubrication and faults in bearing on induction motors through STFT', IEEE 2016 International Conference on Electronics, Communications and Computers (CONIELECOMP), pp. 13-18, Feb. 2016.

[10] Thomson, W. T., Culbert, I.: 'Motor Current Signature Analysis for Induction Motors, Current Signature Analysis for Condition Monitoring of Cage Induction Motors: Industrial Application and Case Histories', Book Chapter, pp. 1-37, John Wiley & Sons, Inc. Hoboken, NJ, USA, Nov. 2016.

[11] Bellini, A., Filippetti, F., Franceschini, G., Tassoni, C., Passaglia, R., Saottini, M., Tontini, G., Giovannini, M., Rossi, A.: 'On-field experience with online diagnosis of large induction motors cage failures using MCSA', IEEE Transactions on Industry Applications, Vol. 38, No. 4, pp. 1045-1053, Jul. 2002.

[12] Martinez, J., Belahcen, A., Arkkio, A.: 'Broken bar indicators for cage induction motors and their relationship with the number of consecutive broken bars', IET Electric Power Applications, Vol. 7, No. 8, pp. 633-642, Sep. 2013.

[13] Antonino-Daviu, J. A., Gyftakis, K. N., Garcia-Hernandez, R., Razik, H., Marques-Cardoso, A. J. M.: 'Comparative influence of adjacent and non-adjacent broken rotor bars on the induction motor diagnosis through MCSA and ZSC methods', 41st Annual IEEE Industrial Electronics Conference (IECON'15), pp. 001680-001685, Nov. 2015.

[14] Khezzar, A., Oumaamar, M. E. K., Hadjami, M., Boucherma, M., Razik, H.: 'Induction motor diagnosis using line neutral voltage signatures', IEEE Transactions on Industrial Electronics, Vol. 56, No. 11, pp. 4581-4591, Nov. 2009.

[15] Hou, Z., Huang, J., Liu, H., Ye, M., Liu, Z., Yang, J.: 'Diagnosis of broken rotor bar fault in open-and closed-loop controlled wye-connected induction motors using zero-sequence voltage', IET Electric Power Applications, Vol. 11, No. 7, pp. 1214-1223, Aug. 2017.

[16] Haddad, R. Z., Strangas, E. G.: 'On the accuracy of fault detection and separation in permanent magnet synchronous machines using MCSA/MVSA and LDA', IEEE Transactions on Energy Conversion, Vol. 31, No. 3, pp. 924-934, Sep. 2016.

[17] Panza, M. A.: 'A Review of Experimental Techniques for NVH Analysis on a Commercial Vehicle', Energy Procedia, 82, pp.1017-1023, Dec. 2015.

[18] Rodriguez, P.J., Belahcen, A., Arkkio A.: 'Signatures of electrical faults in the force distribution and vibration pattern of induction motors', IEE Proceedings – Electric Power Applications, Vol. 153, No. 4, pp. 523-529, Jul. 2006.

[19] Boesing, M., Hofmann, A., De Doncker, R: 'Universal acoustic modelling framework for electrical drives', IET Power Electronics, Vol. 8, No. 5, pp. 693-699, Apr. 2015.

[20] Yazidi, A., Henao, H., Capolino, G. A., Artioli, M., Filippetti, F., Casadei, D.: 'Flux signature analysis: An alternative method for the fault diagnosis of induction machines', IEEE Russia Power Tech, pp. 1-6, Jun. 2005.

[21] Lecointe, J. P., Morganti, F., Zidat, F., Brudny, J. F., Romary, R., Jacq, T., & Streiff, F: 'Effects of external yoke and clamping-plates on AC motor external field', IET Science, Measurement & Technology, Vol. 6, No. No. 5, pp. 350-356, Sep. 2012.

[22] Antonino-Daviu, J. A., Razik, H., Quijano-Lopez, A., Climente-Alarcon, V.: 'Detection of rotor faults via transient analysis of the external magnetic field', 43rd Annual IEEE Industrial Electronics Conference (IECON'17), pp. 3815-3821, Oct. 2017.

[23] Antonino-Daviu, J., Quijano-López, A., Climente-Alarcon, V., Razik, H.: 'Evaluation of the detectability of rotor faults and eccentricities in induction motors via transient analysis of the stray flux', IEEE Energy Conversion Congress and Exposition (ECCE), pp. 3559-3564, Oct. 2017.

[24] Le Besnerais, J., Souron, Q.: 'Effect of magnetic wedges on electromagnetically-induced acoustic noise and vibrations of electrical machines', IEEE XXII International Conference on Electrical Machines (ICEM), pp. 2217-2222, Sep. 2016.

[25] Cheraghi, M., Karimi, M., & Booin, M. B.: 'An investigation on acoustic noise emitted by induction motors due to magnetic sources', IEEE 9th Annual Power Electronics, Drives Systems and Technologies Conference (PEDSTC), pp. 104-109, Feb. 2018.

[26] Binojkumar, A. C., B. Saritha, and G. Narayanan: 'Acoustic noise characterization of space-vector modulated induction motor drives — An experimental approach ', IEEE Transactions on Industrial Electronics, Vol. 62, No. 6, pp. 3362-3371, Jun. 2015.

[27] Benbouzid, M. E. H., & Kliman, G. B.: 'What stator current processing-based technique to use for induction motor rotor faults diagnosis?', IEEE Transactions on Energy Conversion, Vol. 18, No. 2, pp. 238-244, Jun. 2003.

[28] Bellini, A., Filippetti, F., C. Tassoni, Capolino, G.A.: 'Advances in diagnostic techniques for induction machines', IEEE Transactions on Industrial Electronics, Vol. 55, No. 12, pp. 4109-4126, Dec. 2008.

[29] Henao, H., Capolino, G.A., Fernandez-Cabanas, M., Filippetti, F., Bruzzese, C., Strangas, E., Pusca, R., Estima, J., Riera-Guasp, M., Hedayati-Kia, S.: 'Trends in fault diagnosis for electrical machines: A review of diagnostic techniques', IEEE Industrial Electronics Magazine, Vol. 8, No. 2, pp. 31-42, Jun. 2014.

[30] Jiang, C., Li, S., & Habetler, T. G.: 'A review of condition monitoring of induction motors based on stray flux', IEEE Energy Conversion Congress and Exposition (ECCE), pp. 5424-5430, Oct. 2017.

[31] Climente-Alarcon, V., Antonino-Daviu, J. A., Riera-Guasp, M., & Vlcek, M.: 'Induction motor diagnosis by advanced notch FIR filters and the Wigner–Ville distribution', IEEE Transactions on Industrial Electronics, Vol. 61, No. 8, pp. 4217-4227, Aug. 2014.

[32] Martinez-Herrera, A. L., Ledesma-Carrillo, L. M., Lopez-Ramirez, M., Salazar-Colores, S., Cabal-Yepez, E., & Garcia-Perez, A.: 'Gabor and the Wigner-Ville transforms for broken rotor bars detection in induction motors', IEEE 2014 International Conference on Electronics, Communications and Computers (CONIELECOMP), pp. 83-87, Feb. 2014.

[33] Georgoulas, G., Climente-Alarcon, V., Dritsas, L., Antonino-Daviu, J. A., & Nikolakopoulos, G.: 'Start-up analysis methods for the diagnosis of rotor asymmetries in induction motors-seeing is believing', IEEE 24th Mediterranean Conference on Control and Automation (MED), pp. 372-377, Jun. 2016.

[34] Wang, C., Zhou, Z., Unsworth, P. J., & OFarrell, T.: 'Sensorless speed measurement of induction machines using short time Fourier transformation', IEEE International Symposium on Power Electronics, Electrical Drives, Automation and Motion (SPEEDAM), pp. 1114-1119, Jun. 2008.

[35] Kia, S. H., Henao, H., Capolino, G. A., & Martis, C.: 'Induction machine broken bars fault detection using stray flux after supply

disconnection', 32nd Annual IEEE Industrial Electronics Conference (IECON'06), pp. 1498-1503, Nov. 2006.

[36] Cabal-Yepez, E., Garcia-Ramirez, A. G., Romero-Troncoso, R. J., Garcia-Perez, A., & Osornio-Rios, R. A.: 'Reconfigurable monitoring system for time-frequency analysis on industrial equipment through STFT and DWT', IEEE Transactions on Industrial Informatics, Vol. 9, No. 2, pp. 760-71, May 2013.

[37] Gao, R. X., Yan, R.: 'Chapter 2, From Fourier Transform to Wavelet Transform: A Historical Perspective', in Springer, Boston, M.A.: 'Wavelets: Theory and Applications for Manufacturing', pp. 17-32, 2011.

[38] Hon, T. K.: 'Time-frequency analysis and filtering based on the Short-Time Fourier Transform', PhD Dissertation, King's College London, UK, 2013.

[39] Tsoumas, I. P., Georgoulas, G., Mitronikas, E. D., Safacas, A. N.: 'Asynchronous machine rotor fault diagnosis technique using complex wavelets', IEEE Transactions on Energy Conversion, Vol. 23, No. 2, pp. 444-459, Jun. 2008.

[40] Harris, F.J.: 'Windows, harmonic analysis, and the discrete Fourier transform, Rep.', NUC TP532, Nay. Undersea Center, San Diego, California, 1969.

[41] Harris, F.J.: 'On the use of windows for harmonic analysis with the discrete Fourier transform', Proceedings of the IEEE, Vol. 66, No. 1, pp. 51-83, Jan. 1978.
[42] Cohen, L., Lee, C.: 'Local bandwidth and optimal windows for the short time Fourier transform', Advanced Algorithms and Architectures for Signal Processing IV, Vol. 1152, pp. 401-426, International Society for Optics and Photonics, Nov. 1989.

[43] Wang, L. H., Zhang, Q. D., Zhang, Y. H., & Zhang, K.: 'The Time-Frequency Resolution of Short Time Fourier Transform Based on Multi-Window Functions', Advanced Materials Research, Vol. 214, pp. 122-127, Trans Tech Publications, 2011.

[44] Mateo, C., Talavera, J. A.: 'Short-time Fourier Transform with the window size fixed in the frequency domain', Elsevier Digital Signal Processing, pp. 13-21, Jun. 2018.

[45] Turoň, V., 'A study of parameters setting of the STADZT', Acta Polytechnica, Vol. 52, No. 5, pp. 106-111, Jan. 2012.

[46] Qaisar, S. M., Fesquet, L., Renaudin, M.: 'An adaptive resolution computationally efficient short-time Fourier transform', Hindawi Publishing Corporation, Journal of Electrical and Computer Engineering, Research Letters in Signal Processing, Volume 2008, Article ID 932068, May 2008.

[47] Putland, G. R., & Boashash, B., 'Can a signal be both monocomponent and multicomponent?', Australasian Workshop on Signal Processing Applications (WoSPA 2000), pp. 14-15, Dec. 2000.

[48] Cohen, L., 'Time-frequency analysis', Vol. 778, Prentice Hall PTR, Upper Saddle River, New Jersey, USA, ISBN: 0-13-594532-1, 1995.

[49] Boashash, B., 'Time-frequency signal analysis and processing: a comprehensive reference' (1st Edition: 2003), Elsevier, Academic Press, Dec. 2015.

[50] Concari, C., Franceschini, G., & Tassoni, C.: 'Induction machine current space vector features to effectively discern and quantify rotor faults and external torque ripple', IET Elec. Power Applications, Vol. 6, No. 6, Jul. 2012.

[51] Stefani, A., Bellini, A., Filippetti, F.: 'Diagnosis of induction machines' rotor faults n time-varying conditions', IEEE Transactions on Industrial Electronics, Vol. 56, No. 11, pp. 4548-4556, Nov. 2009.

[52] Gritli, Y., Zarri, L., Mengoni, M., Rossi, C., Filippetti, F., Casadei, D.: 'Rotor fault diagnosis of wound rotor induction machine for wind energy conversion system under time-varying conditions based on optimized wavelet transform analysis', IEEE 15th European Conference on Power Electronics and Applications (EPE), pp. 1-9, Sep. 2013

[53] Panagiotou, P.A., Arvanitakis, I., Lophitis, N., Antonino, J.A., Gyftakis, K.N.: 'Analysis of Stray Flux Spectral Components in Induction Machines Under Rotor Bar Breakages at Various Locations', In IEEE 2018 XIII International Conference on Electrical Machines (ICEM), pp. 2345-2351, Sep. 2018.

[54] Riera-Guasp, M., Antonino-Daviu, J.A., Capolino, G.A.: 'Advances in Electrical Machine, Power Electronic and Drive Condition Monitoring and Fault Detection: State of the Art', IEEE Transactions on Industrial Electronics, Vol. 62, No. 3, pp. 1746-1759, March 2015.

[55] Filippetti, F., Bellini, A., Capolino, G.A.:'Condition monitoring and diagnosis of rotor faults in induction machines: State of the art and future perspectives', IEEE Workshop on Electrical Machines Design, Control and Diagnosis (WEMDCD), pp. 196-209, pp. 196-209, March 2013.

[56] Ramirez-Nunez, J.A., Antonino-Daviu, J.A., Climente-Alarcon, V., Quijano-Lopez, A., Razik, H., Osornio-Rios, R.A., Romero-Troncoso, R.J.: 'Evaluation of the detectability of electromechanical faults in induction motors via transient analysis of the stray flux', IEEE Transactions on Industry Applications, Vol. 54 No. 5, pp. _4324-_4332, June 2018.

[57] Antonino-Daviu, J., & Popaleny, P.: 'Detection of Induction Motor Coupling Unbalanced and Misalignment via Advanced Transient Current Signature Analysis', In IEEE 2018 XIII International Conference on Electrical Machines (ICEM), pp. 2359-2364, Sep. 2018.